Transient Permian-Triassic euxinia in the southern Panthalassa deep ocean

S.E. Grasby[1], D.P.G. Bond[2], P.B. Wignall[3], R. Yin[4], L.J. Strachan[5] and S. Takahashi[6]

[1]Geological Survey of Canada, 3303 33rd Street NW, Calgary, AB T2L 2A7, Canada
[2]Department of Geography, Environment and Earth Sciences, University of Hull, Hull HU6 7RX, UK
[3]School of Earth and Environment, University of Leeds, Woodhouse Lane, Leeds LS2 9JT, UK
[4]State Key Laboratory of Ore Deposit Geochemistry, Chinese Academy of Sciences, Guiyang 550081, China
[5]School of Environment, University of Auckland, Auckland 1142, New Zealand
[6]Department of Earth and Planetary Science, University of Tokyo, Hongo 7-3-1, Bunkyo-ku 113-0033, Japan

ABSTRACT

Both the duration and severity of deep-water anoxic conditions across the Permian-Triassic mass extinction (PTME) are controversial. Panthalassa Ocean circulation models yield varying results, ranging from a well-ventilated deep ocean to rapidly developing northern-latitude, but not southern-latitude, anoxia in response to Siberian Traps–driven global warming. To address this uncertainty, we examined a southern-paleolatitude pelagic record. Trace metal and pyrite framboid data suggest bottom-water euxinic conditions developed in the southern Panthalassa Ocean at the PTME, coincident with enhanced volcanic activity indicated by Hg geochemistry. While a global ocean euxinic event at the PTME placed extraordinary stress on marine life, southern surface waters appear to have recovered more quickly as radiolarian populations returned several million years before they did in northern Panthalassa.

INTRODUCTION

The Permian-Triassic mass extinction (PTME) and prolonged Early Triassic ecological recovery (Chen and Benton, 2012) are thought to have been driven by recurrent episodes of marine anoxia related to global warming induced by Siberian Traps volcanism (e.g., Wignall and Twitchett, 2002). The record of marine anoxia, however, is largely restricted to northern-latitude continental-margin records from the Tethys and northwestern Pangea, where shallow-water anoxia would have placed the greatest extinction pressures on fauna. However, understanding the full ecologic stress that temperature-dependent hypoxia placed on marine life and models of its recovery require insight into total ocean O_2 loss (Penn et al., 2018). Uranium isotopes and cerium anomaly data reflecting mean global-ocean redox conditions suggest anoxic seafloor area expanded from ~0.2% to somewhere between 17% and 60% across the PTME (Elrick et al., 2017; Song et al., 2012; Zhang et al., 2018). While the extent of anoxia was substantial, these results imply 40%–83% of the seafloor remained oxic. Consistent with this, ocean circulation models suggest that deep waters became at most dysoxic (Winguth and Winguth, 2012), whereas Penn et al. (2018) suggested development of anoxic seafloor was restricted to northern abyssal plains.

Although the Panthalassa ocean covered 70% of Earth's surface, records from it are rare because its ancient seafloor has been subducted. Surviving remnants of equatorial and northern-paleolatitude pelagic deposits, preserved in accretionary terranes in Japan and Canada, provide insight into deep-water anoxia based on geochemical proxies for local redox conditions. Isozaki (1997) and Kato et al. (2002) suggested anoxia developed in the late Permian and persisted until the Middle Triassic, although Fujisaki et al. (2019) argued for well-ventilated bottom waters throughout the late Permian. Others have suggested, based on pyrite framboid size distributions (Wignall et al., 2010) and redox-sensitive trace elements (Takahashi et al., 2014, 2015), that bottom-water euxinia developed only during the PTME interval. Southern-latitude deep-water anoxia was also suggested by Hori et al. (2007), although timing relative to the PTME is uncertain. In general, geochemical records suggest deep-water anoxia was much more widespread than ocean-circulation and uranium-isotope mass-balance models predict.

Uncertainty in the global extent, duration, and severity of deep-ocean anoxia limits our understanding of how global warming associated with the Siberian Traps affected global ocean O_2 levels. To address this knowledge gap, we examined a southern-hemisphere, mid-paleolatitude pelagic sequence utilizing a combined geochemical, petrographic, and sedimentologic approach.

STUDY AREA

We studied the intertidal section at Island Bay (36°46.131′S, 175 00.200′E; World Geodetic System 1984 [WGS84] datum), Waiheke Island, New Zealand (Fig. 1). Upper Permian through Lower Triassic mudstones and cherts (Kiripaka Formation) overlie oceanic crust that has been obducted in an accretionary prism (Spörli et al., 1989). Conodont biostratigraphy and organic carbon stable isotope ($\delta^{13}C_{org}$) data show that the continuously exposed strata span the Changhsingian to Anisian except for the lower Olenekian (Hori et al., 2011). Paleomagnetic data indicate a paleolatitude of ~34°S (Kodama et al., 2007).

METHODS

We measured a sedimentary log, with numbered lithologically distinct units (Fig. 2). Age assignments are from Hori et al. (2011). Samples were collected every 1–20 cm from fresh surfaces exposed by breaking off marine encrusters and weathered rims, then powdered by agate mortar and pestle. Major and trace elements were analyzed on digested powders in a 2:2:1:1 solution of H_2O-HF-$HClO_4$-HNO_3
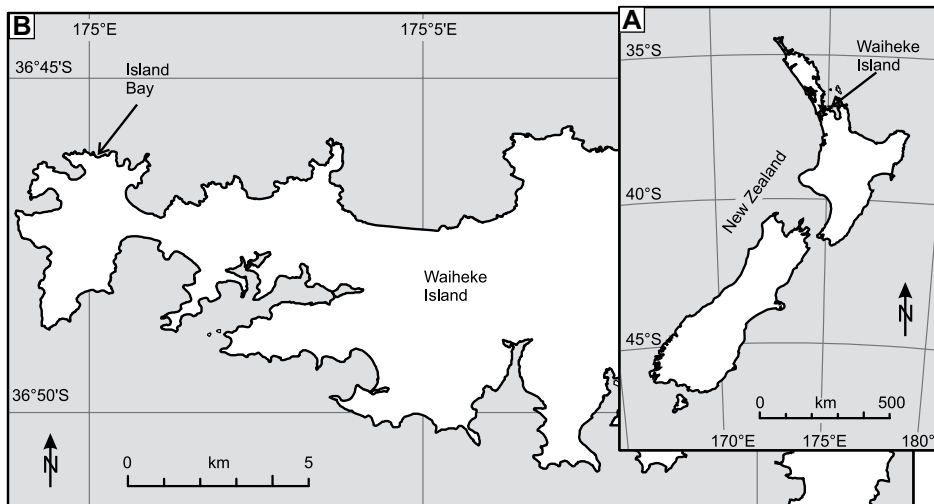

Figure 1. Maps showing the location of Waiheke Island, New Zealand (A), and location of Island Bay (B).

by a PerkinElmer ELAN 9000 mass spectrometer ($\pm$2% error). A LECO AMA254 mercury analyzer was used to measure Hg ($\pm$10%) and total organic carbon (TOC) by HAWK (hydrocarbon analyzer with kinetics) pyrolysis ($\pm$5%). Pyrite framboid size distribution was measured on carbon-coated polished chips on a TESCAN VEGA3 scanning electron microscope.

Samples were acid washed and rinsed with hot distilled water to remove carbonate prior to $\delta^{13}C_{org}$ determination with a Finnigan Mat Delta + XL mass spectrometer interfaced with a Costech 4010 elemental analyzer with $\pm$0.2‰ error. Stable isotopes of Hg were determined using the methods of Grasby et al. (2017) and are expressed in δ^{202}Hg and Δ notations. δ^{202}Hg was defined using the ^{202}Hg/^{198}Hg ratio referenced to the NIST-3133 Hg standard, and the Δ notation was used for the difference between the measured δ^{xxx}Hg and the theoretically predicted δ^{xxx}Hg value, in units of per mil (‰):

$$\Delta^{xxx}Hg = \delta^{xxx}Hg - \delta^{202}Hg \times \beta, \qquad (1)$$

where β is 0.2520 for ^{199}Hg, 0.5024 for ^{200}Hg, and 0.7520 for ^{201}Hg. Analytical results are provided in Table S1 in the Supplemental Material[1].

RESULTS

The stratigraphic section begins with red mudstones that pass into younger gray-green mudstone and then gray, laminated siliceous mudstone. In addition to three black shales (units 5, 7, and 9 in Fig. 2), siliceous mudstones persist across the Permian-Triassic boundary

to the end Induan (4.2 m). Spathian conodonts occur immediately above the Induan-Olenekian boundary, suggesting that the Smithian here is either highly condensed or cut by layer-parallel faulting (Hori et al., 2011). The lowest Olenekian strata consist of 2-cm-thick interbeds of siliceous mudstone and mudstone; both lithologies are gray-green in the lower 80 cm (unit 11). Above unit 11, the siliceous mudstones become red while the interbedded mudstones remain gray-green (unit 12). Around the Olenekian-Anisian boundary and a short distance above a 30-cm-thick siliceous mudstone (unit 13), all beds become red regardless of lithology (Fig. 2). No radiolarians are present in the Changhsingian strata, but they appear in the Lower Triassic siliceous mudstones, forming radiolarian-rich chert beds ~5–10 mm thick, interbedded with finely laminated intervals (Fig. 3). This style of interbedding persists into the Anisian strata.

The $\delta^{13}C_{org}$ values in units 1–3 vary from –28‰ to –26‰, falling in the latest Changhsingian to –30‰ to –28‰ in unit 4, and then to –34‰ in the 20-cm-thick black shale of unit 5, before increasing to ~–30‰ up to the latest Induan. The $\delta^{13}C_{org}$ values further increase to –25‰ at the level where Spathian conodonts appear, and then are variable, but with a general increasing trend, through the Olenekian to a maximum of –22‰ (Fig. 2). The marked late Smithian negative $\delta^{13}C_{org}$ excursion (e.g., Grasby et al., 2013) is not present at Island Bay, supporting the Hori et al. (2011) conclusion that this level is absent.

In the basal and upper parts of the section, content of redox-sensitive element Mo (absolute and normalized to Al) are close to those of the average shale of Wedepohl (1995) (1.3 ppm and 0.15 ppm/wt%, respectively). Mo/Al values increase from 0.1 to 5.7 ppm/wt% in unit 4 and stay relatively elevated (>1.2 ppm/wt%) up to the top of the Induan (unit 10) before return-

ing to values of <0.2 ppm/wt%. In unit 5, Mo/Al reaches 135 ppm/wt% (~900× that of average shale) (Fig. 2). Both U and U/Al increase in unit 4, exceeding average shale values of 3.7 ppm and 0.42 ppm/wt%, respectively, and stay elevated to unit 10 before declining below average shale values (Fig. 2). In unit 5, U is 5.5–32.9 ppm and U/Al is as much as 31× that of average shale. Th/U ratios are >2 at the base and top of the section but drop to <2 in unit 4 and remain low until unit 10. In unit 5, Th/U ranges from 0.15 to 0.42. Mn values are high in the late Permian (as high as 2900 ppm) and then progressively decline through the late Changhsingian to values <50 ppm in unit 5, maintaining these low values until the top of the Induan before steadily increasing up to the Anisian. Values of TOC range from 0.21 to 0.55 wt% except in unit 5 where TOC exceeds 9 wt%.

Pyrite is absent from the basal and uppermost lithologies but is present and locally abundant as framboids in units 4 through 10 (Fig. 2). Of all the units that contain a statistically valid framboid population, unit 4 has the largest mean and standard deviation of pyrite framboid diameters (Fig. 4). In unit 5, framboids become smaller (<5 μm mean) and less variable in size.

Through most of the section, Hg values range from 50 ppb to below the 1 ppb detection limit. A prominent Hg spike (7590 ppb) occurs at the PTME boundary, and then a lesser spike occurs in unit 9 (1230 ppb) (Fig. 2). Both spikes greatly exceed average Hg values (62.4 ppb) in sedimentary rock (Grasby et al., 2019). These spikes survive normalization to TOC, Al, and total sulfur, showing that they are not related to changes in Hg sequestration (Grasby et al., 2019) but represent excess Hg deposition. Background Hg concentrations were too low for stable isotope analyses, but the Hg spikes at the PTME horizon show δ^{202}Hg values ranging from –1.52‰ to –0.97‰ and Δ^{199}Hg values that range from 0.04‰ to 0.09‰, with the exception of a single sample with a Δ^{199}Hg value of –0.07‰ (Fig. 2).

DISCUSSION

The end-Permian negative carbon isotope excursion across the PTME at Island Bay and subsequent shift to higher values through the Early Triassic are consistent with carbonate (Payne et al., 2004) and organic carbon (Grasby et al., 2013) records, supporting the premise that Island Bay represents a deep-water record of the PTME.

Low values of Mo/Al and U/Al, high Th/U and Mn, and the absence of pyrite all indicate that the southern Panthalassa deep ocean was oxic until the very end of the late Permian, similar to the trend demonstrated by equatorial deep-water sections (Wignall et al., 2010; Fujisaki et al., 2019) and to the modern deep ocean. However, in the late Changhsingian, increasing
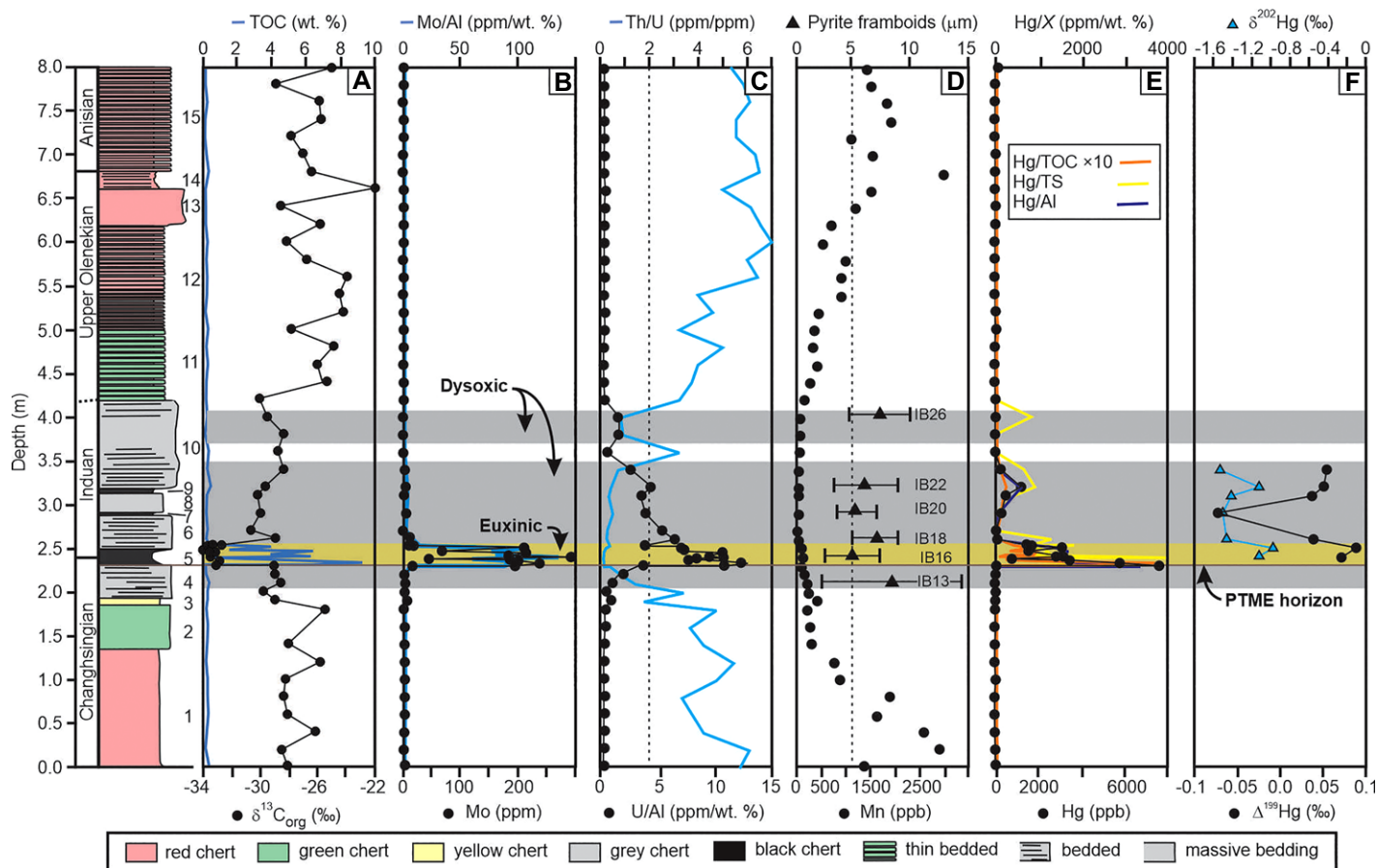
Figure 2. Stratigraphic log from Island Bay, Waiheke Island, New Zealand, with ages from Hori et al. (2011); numbered units are referenced in text. (A) $\delta^{13}C$ values of organic carbon and total organic carbon (TOC). (B) Mo and Mo/Al. (C) U/Al and Th/U. Vertical dashed line represents Th/U = 2, used to define oxic/dusoxic conditions (horizontal gray bars). (D) Mn and the presence of pyrite framboids, with distribution shown as a box and whisker plot. Vertical dashed line represents 5 mm framboid diameter. Sample numbers correspond to Figure 4. (E) Hg and Hg normalized to TOC, total sulfur (TS), and Al. (F) Hg stable isotope data. Δ notation is used for the difference between the measured $\delta^{xxx}Hg$ and the theoretically predicted $\delta^{xxx}Hg$ value. PTME—Permian-Triassic mass extinction.

Mo/Al and U/Al, a fall in Th/U to <2, and the appearance of finely laminated bedding all indicate that deep-water dysoxia developed just prior to the PTME (gray zones in Fig. 2). This is supported by the appearance of pyrite framboids with size ranges that plot in the dysoxic field (Bond and Wignall, 2010) (Fig. 4). The progressive shift to low Mn values suggests development of broader ocean anoxia at the same time (Frakes and Bolton, 1984). Declining oxygen levels prior to the PTME are consistent with other records and are thought to represent the initial emplacement of Siberian Traps magma prior to the main eruption phase that drove extinction (Wignall et al., 2010; Grasby et al., 2013; Burgess et al., 2017).

At the PTME and throughout unit 5, Mo/Al values of as much as 900× average shale values indicate persistently euxinic bottom-water conditions (Lyons et al., 2009) (yellow bar in Fig. 2), as do Th/U ratios as low as 0.15 (Wignall and Twitchett, 1996). Euxinia is supported by pyrite framboid populations with mean diameters <5 μm (Fig. 4), which are characteristic of formation within a H$_2$S-rich water column (Bond and Wignall, 2010). This brief euxinic episode is marked by extraordinarily high TOC (>9 wt%) for deep-sea sediments.

The spike in Hg concentrations is similar to that observed at PTME sections globally and is

Figure 3. Thin-section photograph showing finely laminated siliceous mudstone below and radiolarian-rich level above (4.0 m stratigraphic height at Island Bay, Waiheke Island, New Zealand; Fig. 2). Small fractures offset lamination to a minor extent.
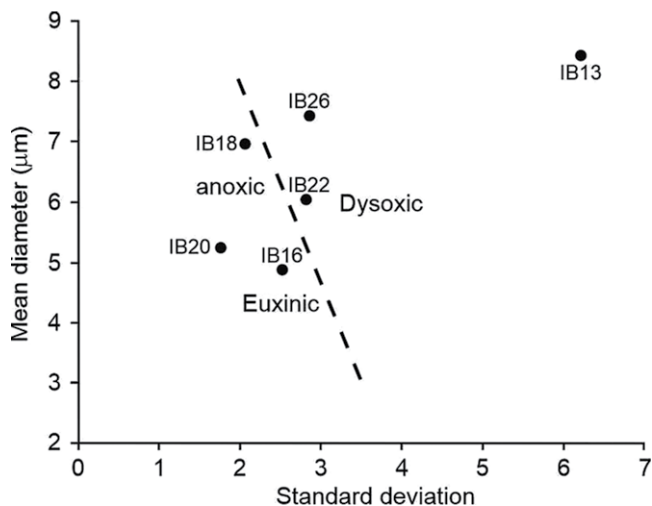
Figure 4. Plot of mean pyrite framboid diameter versus standard deviation relative to fields for euxinic and dysoxic conditions (Bond and Wignall, 2010). Sample numbers correspond to Figure 2.

CONCLUSIONS

The southern Panthalassa Ocean was well ventilated during the late Permian until oxygen-poor conditions developed just prior to the PTME that transitioned to euxinic conditions across the PTME. While oxygenation slightly improved following the PTME, the deep ocean remained largely anoxic until more ventilated conditions returned in the Olenekian. The PTME deep-ocean euxinic event, developed in both the southern and northern hemispheres, reflects much greater net O_2 loss then models predict and must have placed extraordinary stress on marine life. After this event, southern surface waters were more favorable for pelagic life, as testified by the intermittent reappearance of radiolarian populations several million years before they returned in northern Panthalassa. Although the models of Penn et al. (2018) predict anoxia in northern-latitude oceans, they do not replicate the complex ocean redox history presented in the rock record. Full understanding of oxygen stress and recovery requires incorporation of these transient, and potentially devastating, euxinic events into global ocean biogeochemical models.

thought to mark emissions of the Siberian Traps (Grasby et al., 2019; Sanei et al., 2012). The low δ^{202}Hg and more positive Δ^{199}Hg values at Island Bay are similar to modern open-ocean values (Meng et al., 2019) as well as ancient marine sediments (Grasby et al., 2019) where Hg loading is dominated by atmospheric deposition. The Hg spikes have slightly positive Δ^{199}Hg during the PTME, similar to other deep-water PTME records (e.g., Grasby et al., 2017; Wang et al., 2019), supporting that enhanced Hg loading into the southern Panthalassa Ocean had a volcanic source. One negative Δ^{199}Hg value not related to a Hg spike is possibly a signal of enhanced biomass burning after reduction of the dominant volcanic input (Grasby et al., 2017). The Hg data thus support that onset of deep-water euxinia was coincident with the Siberian Traps eruption.

Contrary to our findings, ocean circulation models imply seafloor anoxia was limited to shallower and northern waters (Winguth and Winguth, 2012; Penn et al., 2018), and U mass-balance models are not consistent with extensive deep-water anoxia. Algeo et al. (2011) also suggested that a Japanese section developed only "suboxic to weakly anoxic" conditions at the seafloor. However, Takahashi et al. (2014) argued geochemical proxies from the same section imply euxinia and suggested the low sample density of Algeo et al. (2011) missed the brief euxinic interval. Proxies for local anoxia, including pyrite framboid and trace metal data, indicate anoxia and/or euxinic conditions for other equatorial and northern-latitude Panthalassa deep-water sections across the PTME (Isozaki, 1997; Wignall et al., 2010; Takahashi et al., 2014). Our results indicate that intense euxinia extended into the southern Panthalassa deep seafloor as well. One resolution for the contradiction between model results and observations is that unit 5 represents an extreme, but transient, anoxic event. The very high TOC levels suggest there was prolific primary production that could reflect ocean fertilization from

volcanic fallout. Circulation model simulations may not capture such dynamic redox changes as they reach steady-state conditions, and the existing U isotope records may not resolve such transient events.

The redox history of the global ocean following the PTME is unclear, although oxygen-poor conditions seem to have prevailed (Isozaki, 1997; Wignall and Twitchett, 2002; Grasby et al., 2013). Variations of δ^{238}U suggest intensification of anoxia in the Dienerian and late Spathian (Zhang et al., 2018), with the latter event being strongly developed in equatorial Panthalassa (Wignall et al., 2010; Takahashi et al., 2015) and likely manifest in the Tethyan Ocean (Li et al., 2019). At Island Bay, trace metal enrichment, populations of small pyrite framboids, and low Mn values all indicate oxygen restriction persisted, albeit less intensely, until the Induan, after which oxygenation gradually improved into the Middle Triassic. A temporary loss of framboids and increase of Th/U at ~3.6 m section height may record the short improvement in ocean ventilation in the late Griesbachian seen elsewhere (Fig. 2). However, the late Spathian anoxic event seen in northern Panthalassa is not recorded at Island Bay, unless the drop in Mn values at ~6 m height is a subtle signature.

The PTME also led to the disappearance of radiolarian cherts from northern Panthalassa throughout the Early Triassic "chert gap" of Racki (1999). However, radiolarian chert continued to accumulate in southern Panthalassa, including at Island Bay (Hori et al., 2007). In the Griesbachian, radiolarian populations were a combination of a few surviving Permian holdovers and new taxa. Radiolarian productivity fluctuated considerably, with radiolarian-rich intervals alternating with radiolarian-poor ones (Fig. 3). Given the low Early Triassic sedimentation rate at Island Bay (<1 mm/k.y.), extremely high-productivity intervals likely lasted several thousand years.

REFERENCES CITED

Algeo, T.J., Kuwahara, K., Sano, H., Bates, S., Lyons, T., Elswick, E., Hinnov, L., Ellwood, B., Moser, J., and Maynard, J.B., 2011, Spatial variation in sediment fluxes, redox conditions, and productivity in the Permian–Triassic Panthalassic Ocean: Palaeogeography, Palaeoclimatology, Palaeoecology, v. 308, p. 65–83, https://doi.org/10.1016/j.palaeo.2010.07.007.

Bond, D.P.G., and Wignall, P.B., 2010, Pyrite framboid study of marine Permian–Triassic boundary sections: A complex anoxic event and its relationship to contemporaneous mass extinction: Geological Society of America Bulletin, v. 122, p. 1265–1279, https://doi.org/10.1130/B30042.1.

Burgess, S.D., Muirhead, J.D., and Bowring, S.A., 2017, Initial pulse of Siberian Traps sills as the trigger of the end-Permian mass extinction: Nature Communications, v. 8, 164, https://doi.org/10.1038/s41467-017-00083-9.

Chen, Z.-Q., and Benton, M.J., 2012, The timing and pattern of biotic recovery following the end-Permian mass extinction: Nature Geoscience, v. 5, p. 375–383, https://doi.org/10.1038/ngeo1475.

Elrick, M., Polyak, V., Algeo, T.J., Romaniello, S., Asmerom, Y., Herrmann, A.D., Anbar, A.D., Zhao, L., and Chen, Z.-Q., 2017, Global-ocean redox variation during the middle-late Permian through Early Triassic based on uranium isotope and Th/U trends of marine carbonates: Geology, v. 45, p. 163–166, https://doi.org/10.1130/G38585.1.

Frakes, L.A., and Bolton, B.R., 1984, Origin of manganese giants: Sea-level change and anoxic-oxic history: Geology, v. 12, p. 83–86, https://doi.org/10.1130/0091-7613(1984)12<83:OOMGSC>2.0.CO;2.

Fujisaki, W., Sawaki, Y., Matsui, Y., Yamamoto, S., Isozaki, Y., and Maruyama, S., 2019, Redox con-

dition and nitrogen cycle in the Permian deep mid-ocean: A possible contrast between Panthalassa and Tethys: Global and Planetary Change, v. 172, p. 179–199, https://doi.org/10.1016/j.gloplacha.2018.09.015.

Grasby, S.E., Beauchamp, B., Embry, A.F., and Sanei, H., 2013, Recurrent Early Triassic ocean anoxia: Geology, v. 41, p. 175–178, https://doi.org/10.1130/G33599.1.

Grasby, S.E., Shen, W., Yin, R., Gleason, J.D., Blum, J.D., Lepak, R.F., Hurley, J.P., and Beauchamp, B., 2017, Isotopic signatures of mercury contamination in latest Permian oceans: Geology, v. 45, p. 55–58, https://doi.org/10.1130/G38487.1.

Grasby, S.E., Them, T.R., Chen, Z., Yin, R., and Ardakani, O.H., 2019, Mercury as a proxy for volcanic emissions in the geologic record: Earth-Science Reviews, v. 196, p. 102880, https://doi.org/10.1016/j.earscirev.2019.102880.

Hori, R.S., Higuchi, Y., Fujiki, T., Maeda, T., and Ikehara, M., 2007, Geochemistry of the Oruatemanu Formation, Arrow Rocks, Northland, New Zealand, in Spörli, K.B., et al., eds., The Oceanic Permian/Triassic Boundary Sequence at Arrow Rocks (Oruatemanu), Northland, New Zealand: Lower Hutt, New Zealand, GNS Science Monograph 24, p. 123–156.

Hori, R.S., et al., 2011, Early Triassic (Induan) Radiolaria and carbon-isotope ratios of a deep-sea sequence from Waiheke Island, North Island, New Zealand: Palaeoworld, v. 20, p. 166–178, https://doi.org/10.1016/j.palwor.2011.02.001.

Isozaki, Y., 1997, Permo-Triassic boundary superanoxia and stratified superocean: Records from lost deep sea: Science, v. 276, p. 235–238, https://doi.org/10.1126/science.276.5310.235.

Kato, Y., Nakao, K., and Isozaki, Y., 2002, Geochemistry of Late Permian to Early Triassic pelagic cherts from southwest Japan: Implications for an oceanic redox change: Chemical Geology, v. 182, p. 15–34, https://doi.org/10.1016/S0009-2541(01)00273-X.

Kodama, K., Fukuoka, M., Aita, Y., Sakai, T., Hori, R.S., Takemura, A., Campbell, H.J., Hollis, C.J., Grant-Mackie, J.A., and Spörli, K.B., 2007, Paleomagnetic results from Arrow Rocks in the framework of paleomagnetism in pre-Neogene rocks from New Zealand, in Spörli, K.B., et al., eds., The Oceanic Permian/Triassic Boundary Sequence at Arrow Rocks (Oruatemanu), Northland, New Zealand: Lower Hutt, New Zealand, GNS Science Monograph 24, p. 177–196.

Li, M., Song, H., Wignall, P.B., She, Z., Dai, X., Song, H., and Xiao, Q., 2019, Early Triassic oceanic red beds coupled with deep sea oxidation in South Tethys: Sedimentary Geology, v. 391, p. 105519, https://doi.org/10.1016/j.sedgeo.2019.105519.

Lyons, T.W., Anbar, A.D., Severmann, S., Scott, C., and Gill, B.C., 2009, Tracking euxinia in the ancient ocean: A multiproxy perspective and Proterozoic case study: Annual Review of Earth and Planetary Sciences, v. 37, p. 507–534, https://doi.org/10.1146/annurev.earth.36.031207.124233.

Meng, M., Sun, R.-y., Liu, H.-w., Yu, B., Yin, Y.-g., Hu, L.-g., Shi, J.-b., and Jiang, G.-b., 2019, An integrated model for input and migration of mercury in Chinese coastal sediments: Environmental Science & Technology, v. 53, p. 2460–2471, https://doi.org/10.1021/acs.est.8b06329.

Payne, J.L., Lehrmann, D.J., Wei, J., Orchard, M.J., Schrag, D.P., and Knoll, A.H., 2004, Large perturbations of the carbon cycle during recovery from the end-Permian extinction: Science, v. 305, p. 506–509, https://doi.org/10.1126/science.1097023.

Penn, J.L., Deutsch, C., Payne, J.L., and Sperling, E.A., 2018, Temperature-dependent hypoxia explains biogeography and severity of end-Permian marine mass extinction: Science, v. 362, eaat1327, https://doi.org/10.1126/science.aat1327.

Racki, G., 1999, Silica-secreting biota and mass extinctions: Survival patterns and processes: Palaeogeography, Palaeoclimatology, Palaeoecology, v. 154, p. 107–132, https://doi.org/10.1016/S0031-0182(99)00089-9.

Sanei, H., Grasby, S.E., and Beauchamp, B., 2012, Latest Permian mercury anomalies: Geology, v. 40, p. 63–66, https://doi.org/10.1130/G32596.1.

Song, H., Wignall, P.B., Tong, J., Bond, D.P.G., Song, H., Lai, X., Zhang, K., Wang, H., and Chen, Y., 2012, Geochemical evidence from bio-apatite for multiple oceanic anoxic events during Permian–Triassic transition and the link with end-Permian extinction and recovery: Earth and Planetary Science Letters, v. 353–354, p. 12–21, https://doi.org/10.1016/j.epsl.2012.07.005.

Spörli, K.B., Aita, Y., and Gibson, G.W., 1989, Juxtaposition of Tethyan and non-Tethyan Mesozoic radiolarian faunas in melanges, Waipapa terrane, North Island, New Zealand: Geology, v. 17, p. 753–756, https://doi.org/10.1130/0091-7613(1989)017<0753:JOTANT>2.3.CO;2.

Takahashi, S., Yamasaki, S.-i., Ogawa, Y., Kimura, K., Kaiho, K., Yoshida, T., and Tsuchiya, N., 2014,

Bioessential element-depleted ocean following the euxinic maximum of the end-Permian mass extinction: Earth and Planetary Science Letters, v. 393, p. 94–104, https://doi.org/10.1016/j.epsl.2014.02.041.

Takahashi, S., Yamasaki, S.-i., Ogawa, K., Kaiho, K., and Tsuchiya, N., 2015, Redox conditions in the end-Early Triassic Panthalassa: Palaeogeography, Palaeoclimatology, Palaeoecology, v. 432, p. 15–28, https://doi.org/10.1016/j.palaeo.2015.04.018.

Wang, X., Cawood, P.A., Zhao, H., Zhao, L., Grasby, S.E., Chen, Z.-Q., and Zhang, L., 2019, Global mercury cycle during the end-Permian mass extinction and subsequent Early Triassic recovery: Earth and Planetary Science Letters, v. 513, p. 144–155, https://doi.org/10.1016/j.epsl.2019.02.026.

Wedepohl, K.H., 1995, The composition of the continental crust: Geochimica et Cosmochimica Acta, v. 59, p. 1217–1232, https://doi.org/10.1016/0016-7037(95)00038-2.

Wignall, P.B., and Twitchett, R.J., 1996, Oceanic anoxia and the end Permian mass extinction: Science, v. 272, p. 1155–1158, https://doi.org/10.1126/science.272.5265.1155.

Wignall, P.B., and Twitchett, R.J., 2002, Extent, duration, and nature of the Permian-Triassic superanoxic event, in Koeberl, C., and MacLeod, K.G., eds., Catastrophic Events and Mass Extinctions: Impacts and Beyond: Geological Society of America Special Paper 356, p. 395–413, https://doi.org/10.1130/0-8137-2356-6.395.

Wignall, P.B., Bond, D.P.G., Kuwahara, K., Kakuwa, Y., Newton, R.J., and Poulton, S.W., 2010, An 80 million year oceanic redox history from Permian to Jurassic pelagic sediments of the Mino-Tamba terrane, SW Japan, and the origin of four mass extinctions: Global and Planetary Change, v. 71, p. 109–123, https://doi.org/10.1016/j.gloplacha.2010.01.022.

Winguth, C., and Winguth, A.M.E., 2012, Simulating Permian–Triassic oceanic anoxia distribution: Implications for species extinction and recovery: Geology, v. 40, p. 127–130, https://doi.org/10.1130/G32453.1.

Zhang, F., Romaniello, S.J., Algeo, T.J., Lau, K.V., Clapham, M.E., Richoz, S., Herrmann, A.D., Smith, H., Horacek, M., and Anbar, A.D., 2018, Multiple episodes of extensive marine anoxia linked to global warming and continental weathering following the latest Permian mass extinction: Science Advances, v. 4, e1602921, https://doi.org/10.1126/sciadv.1602921.